Gamma Ray on Superjunction MOSFET and Gate Ringing

Sangyun Song, Dong-seok Kim, and Hyemin Kang, *Member, IEEE*

Abstract—**Superjunction MOSFETs used in aircraft and spacecraft can be exposed to high-density and high-energy gamma-ray radiation environments. Commercial superjunction MOSFETs were irradiated with gamma rays in their packaged state and their static and dynamic characteristics were measured. From the double pulse test, the switching waveforms of the devices were extracted as a function of irradiation dose, and gate oscillations were observed. To provide an accurate physical analysis, a five-contact TCAD model was used and compared with the actual data. In the simulation, by dividing the gate into the gate-to-source and the gate-to-drain, and the source into the n^+ and the p^+, we identified the parasitic capacitance characteristics of the device and analyzed the gate oscillations.**

Index Terms—**Gamma ray, gate ringing, power MOSFET, superjunction.**

I. Introduction

POWER electronics have become indispensable in recent industrial, commercial, aerospace, and military applications. As the core of power electronics, power semiconductors are widely used in switching-mode power conversion and control, power amplifiers, and so on [1], [2], [3]. With the recent growth of the aerospace industry, power semiconductors have continued to be developed as a key component in international space stations, satellite power systems, aircraft, and motor drives [1], [4], [5]. The effects of radiation on power semiconductors vary, but the total ionizing dose (TID) effect is dominant because, when power semiconductors are exposed to high-energy electromagnetic radiation such as gamma rays or environments with high-energy particles for

a long period of time, a large amount of charge accumulates in the material [6], [7], [8], [9]. In particular, because power semiconductors consist of metal–oxide–semiconductor (MOS) structures, high-energy radiation is absorbed on the oxide layer. The absorbed energy produces electron–hole pairs, but electrons in the oxides are more mobile than holes, so they are quickly removed by diffusion or electric fields before recombination with holes. The remaining holes, when the positive bias of the gate is applied, move to the interface and form an accumulation of oxide trap charges or interface trap charges [10], [11], [12], [13].

Superjunction MOSFETs can achieve high breakdown voltage and low on-resistance due to the vertical p-n junction structures minimizing power dissipation and enabling high-speed switching [14], [15], [16]. Due to these characteristics, they can be widely used in space applications, making their investigation in radiation environments essential.

Therefore, in this article, we sought to identify distinct differences in the static and dynamic properties of the superjunction device through gamma-irradiation experiments. The commercial superjunction MOSFETs, designed by this group as the detailed parameters of the device are confidential, have a breakdown voltage of 650 V and R_{dson} of 360 mΩ. The package type is TO-220F. Existing studies regarding cosmic ray irradiation on superjunctions have mainly focused on static characteristics, but dynamic switching characteristics have rarely been studied. The switching characteristics, especially for the gate ringing during turn-on and turn-off, are measured by a hand-made double pulse test.

II. Measurement and Simulation

Gamma-ray irradiation doses on the superjunction MOSFETs were 100, 300, 500, 800, and 1000 (Krad) with a Cobalt-60 source at Korea Atomic Energy Research Institute (KAERI).

Fig. 1 shows the experimental setup and equipment for superjunction MOSFETs' switching measurements. The device's current rating was 11 A (360 mΩ) and the 4H-SiC Schottky diode for the freewheeling current used. The 10-Ω external gate resistance was attached to the device under test (DUT) of the superjunction MOSFET with 12-V pulsed gate voltage. The HV input was set to 400 V and the load inductance (L_L) was 0.4 mH.

Fig. 2 shows the circuit used in the five-contact mixed-mode simulation. The five-terminal method divides the gate into the
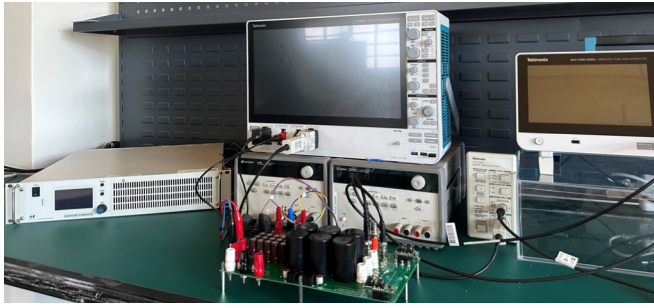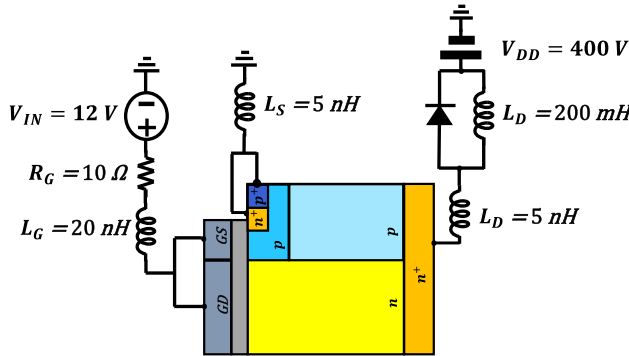
Fig. 1. Test setup for double pulse test.

Fig. 2. Schematic illustration of a five-contact inductive switching configuration using the mixed-mode simulation.

gate-to-source and the gate-to-drain, and the source into the n^+ (the channel current) and the p^+ (the drain-to-source displacement current). The traditional three-terminal (gate, drain, and source) analysis has limitations in examining current movement over time. The five-terminal approach helps to identify "potential shift" due to parasitic inductance during switching on/off and provides an analysis of gate ringing [17]. Simulation results were also compared to actual measurement data.

In the simulated circuit, the gate terminal was configured with a 10-Ω external gate resistor as in the actual measurement and a 20-nH parasitic gate inductance. The parasitic inductances of the drain and the source were set to 5 nH. Depending on the package type and circuit, the parasitic inductance for each terminal of the device can be adjusted from at least 5 nH to about 50 nH. Therefore, the parasitic inductance values of each terminal of the simulation were set individually to match the switching behavior and gate ringing of the actual measurement waveforms. The freewheeling diode in the simulation was also composed of the 4H-SiC Schottky diode with a breakdown voltage of 650 V, just like the actual measurement.

III. STATIC CHARACTERISTICS

The change in the static characteristics with the amount of gamma-ray irradiation is shown in Fig. 3. From the transfer curves [Fig. 3(a)], it is found that the threshold voltage (V_{th}) is negatively shifted. As mentioned above, the change in the threshold voltage is mainly due to the oxide trap charge led by the TID effect [18]. Specifically, the threshold voltages (at 250-μA drain-to-source current) with gamma irradiation doses are 3.30 V (nonirradiation), 1.03 V (100 krad), 0.57 V (300 krad), 0.41 V (500 krad), 0.26 V (800 krad), and 0. 23 V (1 Mrad).
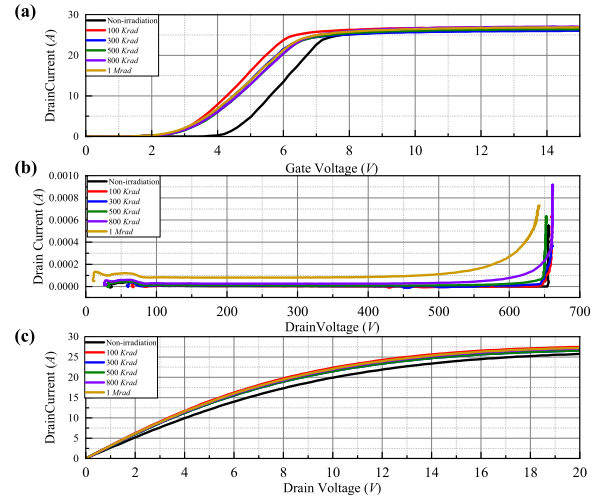

Fig. 3. Static characteristics according to gamma-ray irradiation. (a) Transfer curve. (b) Breakdown voltage. (c) Output curve.
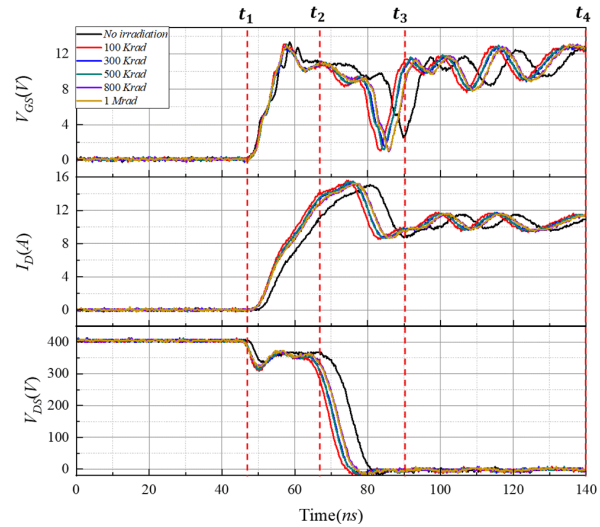

Fig. 4. Actual waveforms of inductive switching of the superjunction MOSFETs during the turn-on transition.

The breakdown voltage is shown in Fig. 3(b), and the leakage current increased as the gamma-ray irradiation increased. This is due to the accumulation of a positive charge in the oxide, which shrinks the depletion region near the channel, allowing current to flow into the channel [19], [20] as well as a higher possibility of punchthrough.

As shown in Fig. 3(c), the output curve was measured under 20-V gate-to-source voltage. A slight decrease in the total resistance was observed in the irradiated device compared to the unirradiated device, which is due to the fact that, as the threshold voltage is lowered, more electron accumulation in the channel is formed at the same gate voltage allowing more current to flow.

IV. TURN-ON ANALYSIS

Fig. 4 shows the measured turn-on inductive switching waveforms as a function of gamma-ray dose. During the turn-on transient, the primary gate ringing occurs in the period t_1-t_2 and the secondary gate ringing occurs in the period t_2 to t_3. Overall, it was found that the dI_S/dt difference with respect
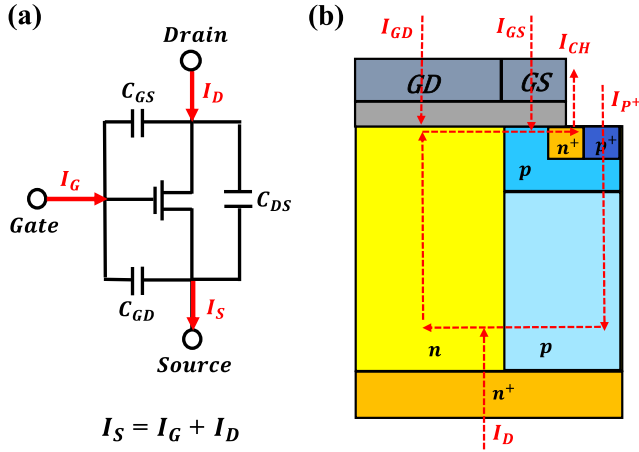
Fig. 5. Schematic illustration of current flow in a superjunction MOSFET at turn-on. (a) Basic circuit with three terminals (gate, drain, and source). (b) Current flow inside five-contact devices using mixed-mode simulation during the turn-on transient period.
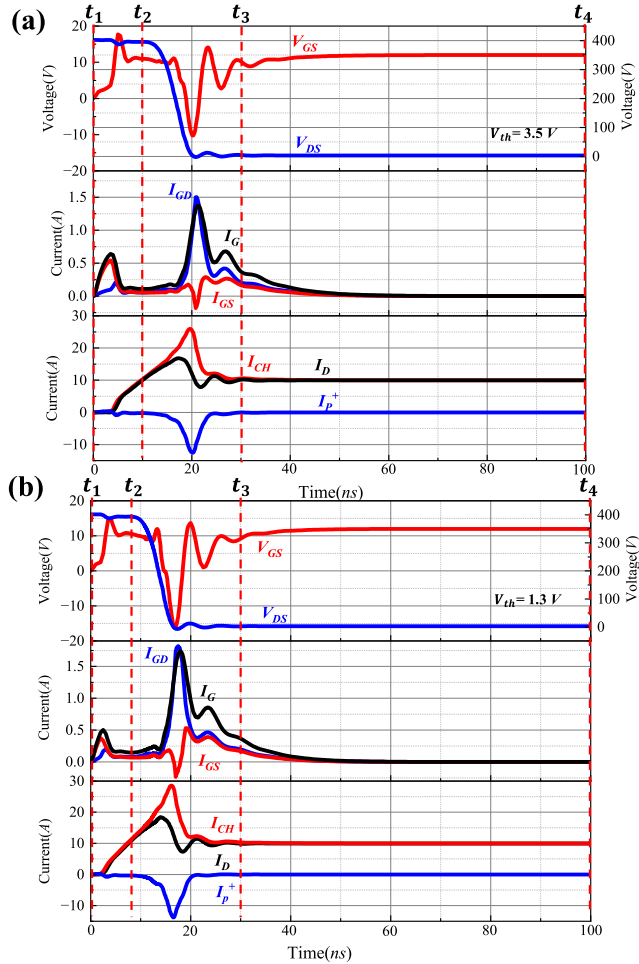

Fig. 6. Simulation of turn-on inductive switching of superjunction MOSFETs. (a) Waveforms with $V_{th} = 3.5$ V. (b) Waveforms with $V_{th} = 1.3$ V.

to the gamma-ray dose affects the degree of secondary gate ringing.

To further analyze these phenomena, turn-on mixed-mode simulations were performed, as shown in Figs. 5 and 6. During the turn-on transient, the source current (I_S) is expressed as the sum of the gate current (I_G) and the drain current (I_D), as shown in Fig. 5(a). The channel current (I_{CH}) through the

n^+ source contact consists of the drain current (I_D), the drain-to-source current (I_{P+}), the gate-to-drain (I_{GD}), and the gate-to-source (I_{GS}). Therefore, the channel current (I_{CH}) for the turn-on transient is derived as follows:

$$I_{CH} = I_{GS} + I_{GD} + I_D - I_{P+}. \quad (1)$$

The gate current (I_G) can be divided into the I_{GS} and the I_{GD} displacement currents to charge the gate-to-source capacitance (C_{GS}) and the the gate-to-drain capacitance (C_{GD}), respectively

$$I_G = I_{GS} + I_{GD}. \quad (2)$$

The source current (I_S) can be divided into the n^+ contact current for electrons and the p^+ contact current for holes

$$I_S = I_{CH} + I_{P+}. \quad (3)$$

t_1-t_2: In Fig. 4 (the measured waveforms), when the pulse voltage is applied to the gate at time t_1, the gate voltage increases as it charges the input capacitance, C_{ISS} ($C_{GS}+C_{GD}$). When the gate voltage reaches V_{th}, the channel is formed and the drain current starts to flow. Gamma-ray irradiated devices have relatively lower V_{th} than the normal (nonirradiation case due to the TID effect [10]. This causes the channel to activate earlier than normal (nonirradiation and the drain current (I_D) flows earlier. Also, in this interval, the gate voltage (V_{GS}) increases instantaneously to 12 V. The simulation in Fig. 6 shows the same trend. As shown in Fig. 7(a), as the source current (I_S) flows, it creates a reverse electromotive force on the parasitic source inductance, resulting in a positive "potential shift" to the source terminal by the amount equal to $L_S \times dI_S/dt$, and the gate potential also experiences the same positive "potential shift" by $L_S \times dI_S/dt$, as shown in Fig. 7(b). Therefore, the potential difference between the input pulse voltage (12 V) and the gate voltage (V_{GS}) decreases rapidly, and the gate current (I_G) drops nearly to zero (around 8 ns in Fig. 6). Therefore, the parasitic RLC circuit on the gate terminal is triggered due to the change in the gate current, dI_G/dt. The parasitic gate inductance $L_G \times dI_G/dt$ and C_{ISS} ($C_{GS} + C_{GD}$) combine to generate primary gate ringing [17].

t_2-t_3: The gate voltage at t_2 after entering the plateau region is [21]

$$V_G(t_2) = V_{GP} = \frac{I_D}{g_m} + V_{th} \quad (4)$$

where V_{GP} is the gate voltage in the plateau region and g_m is the superjunction MOSFET's transconductance [21].

As shown in Fig. 4 (measured data), after t_2, the drain current (I_D) is greater than 11 A (driving current). In the plateau region, while the drain voltage (V_{DS}) slowly decreases, the freewheeling Schottky diode begins to form a depletion region to support 400 V. As a result, the displacement currents from the Schottky diode are added to the drain current, leading to an instantaneous increase in the MOSFET's drain current, as shown in Fig. 8 [22].

As V_{DS} drops to near ON-state voltage (around 80 ns in Fig. 4) and the Schottky diode takes 400 V, the displacement current from the freewheeling Schottky diode rapidly decreases and the drain current also rapidly decreases down
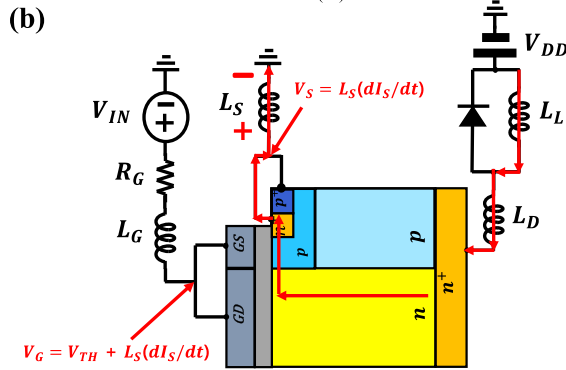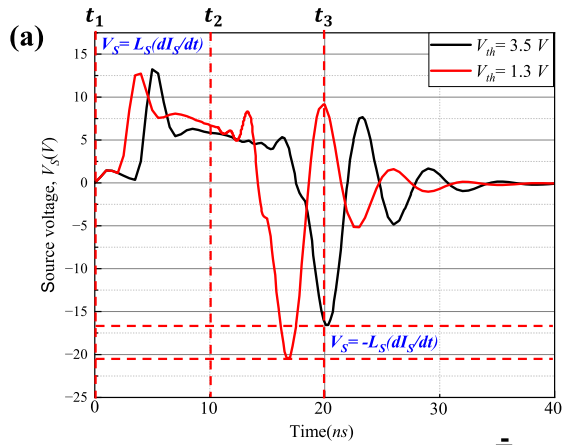
Fig. 7. Simulation of back electromotive force of parasitic source inductance by $L_S \times dI_S/dt$ during the turn-on transient period. (a) Simulation of "potential shift" due to parasitic source inductance during the turn-on transient. (b) Positive "potential shift" during the period t_1-t_2.
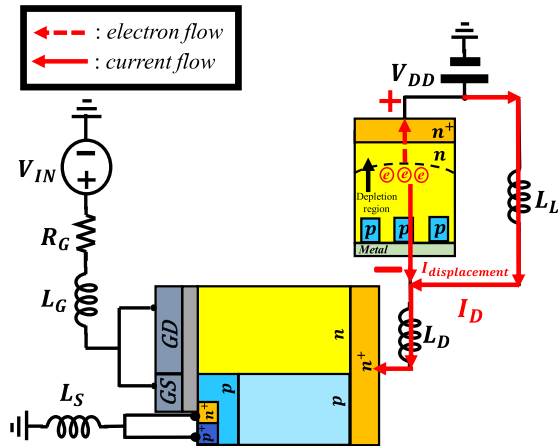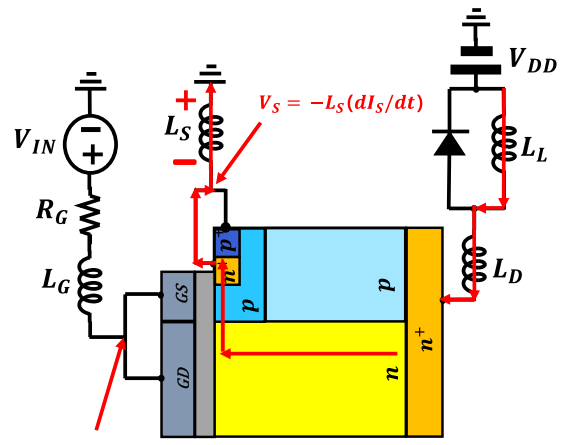

Fig. 8. Mechanism for generating displacement current of the diode during the turn-on transient period in the simulation.

Fig. 9. Negative "potential shift" in parasitic source inductance due to decreasing displacement current during t_2-t_3.
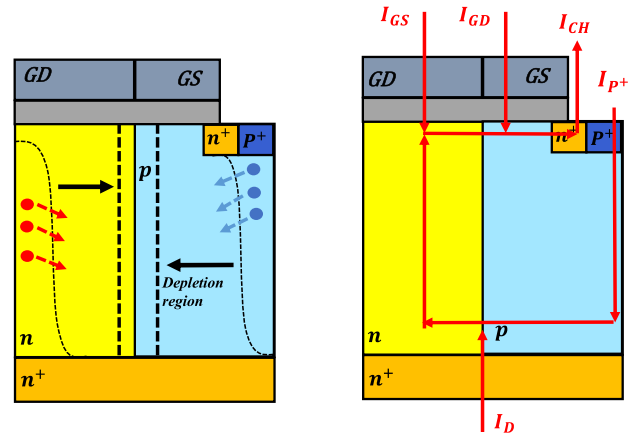

Fig. 10. Current flow according to the movement of electrons (red circle) and holes (blue circle) when the depletion region is released.

irradiated device is higher than that of the nonirradiation device. Similarly, from the simulation, we can also see that the drain current in Fig. 6(b) ($V_{th} = 1.3$ V) is higher than the drain current in Fig. 6(a) ($V_{th} = 3.5$ V).

As the threshold voltage decreases, more electron accumulation in the channel is formed at the same gate voltage, allowing more drain current to flow. Therefore, when the displacement current decreases and the drain current drops to the drive current (11 A), dI_S/dt becomes larger. As shown in Fig. 7(a) (around 18–20 ns), the device with the lower threshold voltage ($V_{th} = 1.3$ V) has a larger negative "potential shift" [17].

There is also a difference in the current flow inside the device with and without gamma-ray irradiation. In Fig. 6 (around 10–20 ns), it can be seen that as the drain voltage decreases, the depletion region inside the device is gradually released, and the displacement current (I_{p+}) of the drain-to-source capacitance (C_{DS}) combines with the drain current leading to an increase of I_{CH}. The schematic current flows are shown in Fig. 10. I_{CH} for $V_{th} = 3.5$ V case [around 18 ns in Fig. 6(b)] is higher than that of $V_{th} = 1.3$ V case [around 20 ns in Fig. 6(a)]. Equation (4) shows that a low threshold voltage lowers the plateau voltage (V_{GP}) and increases the potential difference between the input pulse voltage (12 V) and the gate voltage (V_{GP}). Therefore, the $V_{th} = 1.3$ V case rapidly increases the gate current and C_{Iss} charges faster leading to

to the driving level (11 A). The source current (I_S) change causes the negative "potential shift" by $L_S \times dI_S/dt$ around the 10–20-ns interval in Fig. 7(a). The gate also experiences the negative "potential shift" by $L_S \times dI_S/dt$, as shown in Fig. 9 [17].

The potential difference between the input voltage and the gate voltage (V_{GS}) becomes large and the gate current increases rapidly by dI_G/dt; secondary gate ringing occurs by $L_G \times dI_G/dt$ and C_{ISS} [17]. The degree of secondary gate ringing varies depending on the presence or absence of gamma-ray irradiation. From Fig. 4 (around 75–85 ns), it can be seen that the peak drain current (I_D) of the gamma-ray
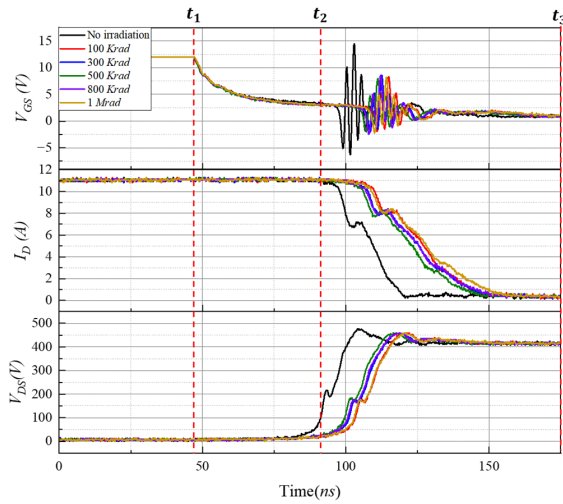
Fig. 11. Actual waveforms of inductive switching of the superjunction MOSFET during the turn-off transition.

more inversion and channel current than that of $V_{th} = 3.5$ V. When V_{DS} reaches the ON-state voltage, the n-pillar and the p-pillar depletion are nearly released, reducing the C_{DS} discharge current (I_{P+}), which also reduces I_{CH}. To reduce I_{CH}, the inversion electrons in the channel must be discharged. This is why I_{GS} is discharged (around 20 ns in Fig. 6). The device with lower V_{th} has more inversion electrons in the channel and, therefore, higher I_{GS} flow out [around 18 ns in Fig. 6(b)]. Since the potential difference between the input pulse voltage and the gate voltage is not high, the discharged I_{GS} current does not flow into the gate driver but flows into the GD terminal as a form of I_{GD} to charge C_{GD}.

$t_3 - t_4$: In this period, the drain current reaches 11 A and dI_S/dt disappears, so the "potential shift" caused by the parasitic inductance is released and the gate ringing diminishes. V_{GS} also reaches 12 V and the turn-on process is terminated.

V. TURN-OFF ANALYSIS

Fig. 11 shows the turn-off waveform of an actual inductive switching as a function of gamma-ray irradiation dose. It can be seen that, during the turn-off transient, the gamma-ray irradiation devices show smaller gate ringing than the non-irradiation device.

To further analyze these phenomena, turn-off mixed-mode simulations were performed, as shown in Figs. 12 and 13.

In the turn-off transient period, the drain current (I_D) is expressed as the sum of the gate current (I_G) and the source current (I_S), as shown in Fig. 12(a). The channel current (I_{CH}) from the n^+ source contact consists of the drain current (I_D), the drain-to-source current (I_{P+}), the gate-to-drain (I_{GD}), and the gate-to-source (I_{GS}). Therefore, the channel current (I_{CH}) of the turn-off transient is derived as follows:

$$I_{CH} = I_D - I_{GS} - I_{GD} - I_{P+}. \tag{5}$$

As opposed to the turn-on transient state, the gate current (I_G) can be divided into the I_{GS} and the I_{GD} displacement currents to discharge C_{GS} and C_{GD}, respectively

$$I_G = I_{GS} + I_{GD}. \tag{6}$$
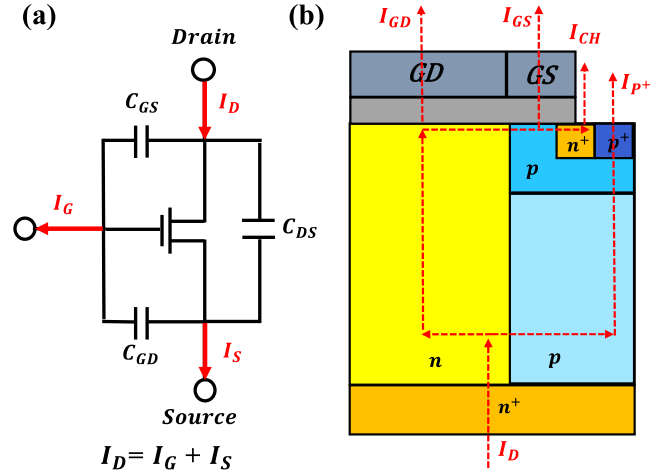
Fig. 12. Schematic illustration of current flow in a superjunction MOSFET at turn-off. (a) Basic circuit with three terminals (gate, drain, and source). (b) Current flow inside five-contact devices using mixed-mode simulation during the turn-off transient period.
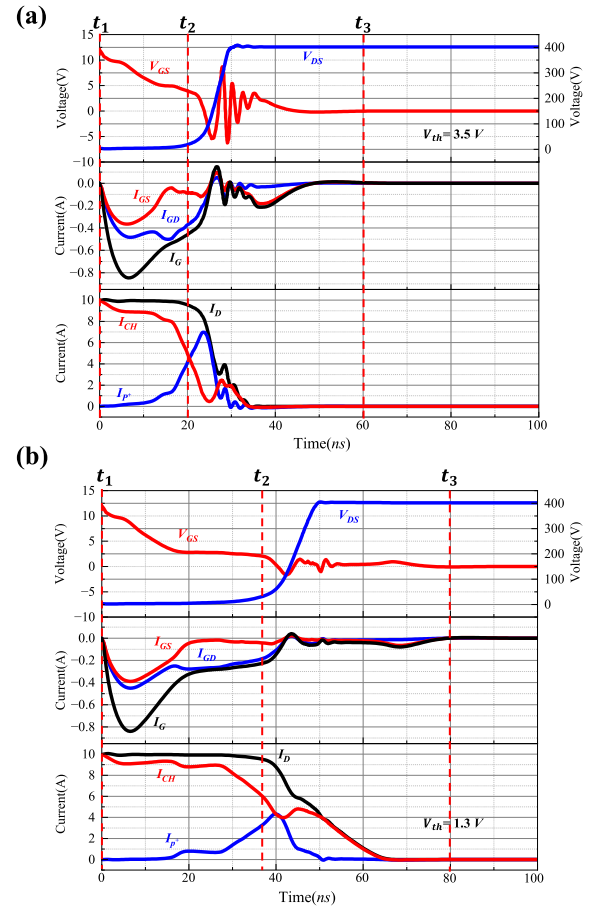
Fig. 13. Simulation of turn-off inductive switching of superjunction MOSFETs. (a) Waveforms with $V_{th} = 3.5$ V. (b) Waveforms with $V_{th} = 1.3$ V.

The source current (I_S) can be divided into the n^+ contact current for electrons and the p^+ contact current for holes

$$I_S = I_{CH} + I_{P+}. \tag{7}$$

Fig. 12(b) shows the current flows in the device during the turn-off transient period, which will be described in detail in the period t_1–t_2. Fig. 13 shows the simulated turn-off

Fig. 14. Current flow according to the movement of electrons (red circle) and holes (blue circle) when the depletion region between n-pillar and p-pillar is enlarged.

Fig. 15. Simulation of back electromotive force of parasitic source inductance $L_S \times dI_S/dt$ by during turn-off transient period. (a) Simulation of "potential shift" due to parasitic source inductance during the turn-off transient. (b) Negative "poential shift" during the period t_2–t_3.

inductive switching with $V_{th} = 3.5$ V (nonirradiation) and 1.3 V (irradiation).
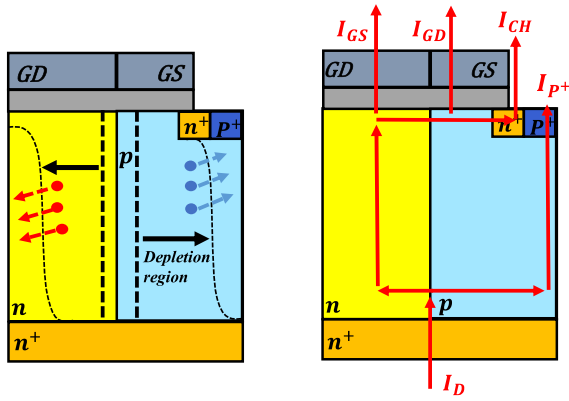
t_1–t_2: In Fig. 13, at point t_1, when the pulse voltage is no longer applied, V_{GS} begins to decrease as the gate current (I_G) begins to discharge from C_{ISS}. According to (4), the plateau voltage (V_{GP}) depends on the threshold voltage (V_{th}). The $V_{th} = 3.5$ V case has a higher V_{GP} than that of $V_{th} = 1.3$ V. The difference in V_{GP} during t_1–t_2 makes the difference in the plateau period. In the case of $V_{th} = 3.5$ V, V_{GP} is higher than that of $V_{th} = 1.3$ V leading to a higher V_{GP}. The higher V_{GP} creates a higher gate-to-drain discharge current (I_{GD}) as well as a faster gate-to-drain potential growth. This results in a shorter plateau period. In the case of $V_{th} = 1.3$ V, I_{GD} discharges slowly because the potential difference between V_{GP} and the ground is relatively small. The slow discharging current of I_{GD} causes a longer plateau period than that of V_{th} (3.5 V).

As shown in Fig. 14, as the gate-to-drain potential rises, the depletion region between the n-pillar and p-pillar expands and a part of the drain current is divided into the displacement current (I_{P+}) to charge the large C_{DS} of the superjunction pillars [around 0–20 ns in Fig. 13(a) and 20–37 ns in Fig. 13(b)]. In this period, since most of the drain current is consumed to charge C_{DS}, I_{p+} increases rapidly, while I_{CH} decreases.

t_2–t_3: In Figs. 11 and 13 (measured and simulated waveforms), the channel current decreases when V_{GS} decreases from V_{GP} to V_{th}. The source current (I_S) in this period creates dI_S/dt. This dI_S/dt creates a back electromotive force on the parasitic source inductance, resulting in a negative "potential shift" on the source terminal by $L_S \times dI_S/dt$, as shown in Fig. 15(a). As shown in Fig. 15(b), there is also a negative "potential shift" to the gate potential by $L_S \times dI_S/dt$. The rapid change in the gate voltage leads to a rapid decrease in the gate current by dI_G/dt. This rapid decrease in the gate current leads to a gate ringing by the combination of C_{ISS} and $L_G \times dI_G/dt$ [17]. However, the gate ringing trend highly depends on the existence of gamma-ray irradiation. As mentioned earlier, the discharging gate current (I_G) is higher in the case of the higher threshold voltage condition ($V_{th} = 3.5$ V, nonirradiation) [Fig. 13(a)] than that of the lower threshold voltage condition [$V_{th} = 1.3$ V, irradiation, Fig. 13(b)].
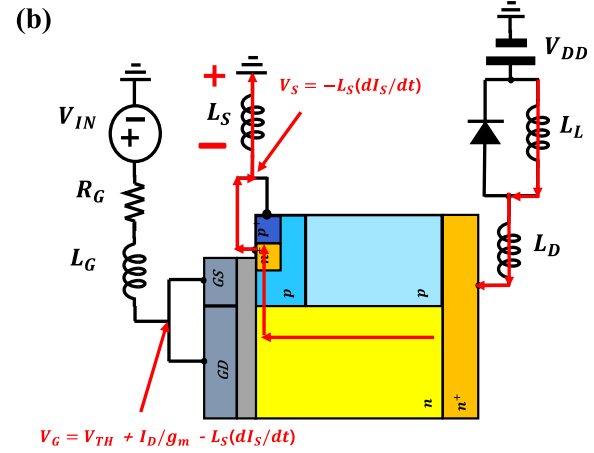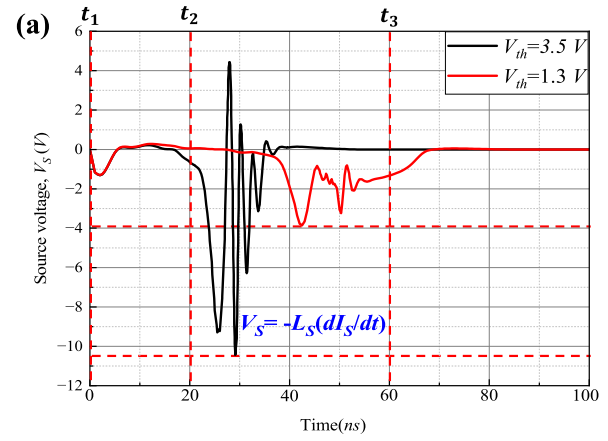
As shown in Fig. 15(b), the gate also experiences a "potential shift" of $L_S \times dI_S/dt$ and, therefore, the higher threshold voltage condition ($V_{th} = 3.5$ V) results in a higher change in the gate current dI_G/dt due to the higher gate voltage change. Therefore, the high V_{th} case (nonirradiation) leads to a higher gate ringing than that of the low V_{th}. In conclusion, devices irradiated with gamma rays during the turn-off transient reduce gate ringing due to the low threshold voltage.

As already mentioned, the $V_{th} = 3.5$ V case produces a higher gate-to-drain discharge current (I_{GD}) and faster gate-to-drain potential growth than $V_{th} = 1.3$ V.

In the case of $V_{th} = 3.5$ V, the depletion region between the n-pillar and the p-pillar is quickly expanded due to the fast drain potential growth. In the meanwhile, since C_{DS} of superjunction MOSFET is very large, most of the drain current is allocated to the displacement current (I_{P+}) to charge C_{DS}. Therefore, the channel current drops to near 1 A, while C_{DS} displacement current rise to near 7 A [around 20–23 ns in Fig. 13(a)]. The continuously increasing V_{DS} leads to the n-pillar and the p-pillar to be completely depleted laterally [around 23 ns in Fig. 13(a)]. The fully depleted pillars present a dramatic decrease in C_{DS} and I_{P+} charging C_{DS} also decreases. Therefore, the drain current is converted into the channel current again (I_{CH}). At the same time, the gate potential drops to approximately -5 V [around 23 ns in Fig. 13(a)] due to the negative "potential shift" of the gate

by $L_S \times dI_S/dt$ as previously mentioned. Therefore, the gate current instantaneously charges C_{ISS}. The channel is further opened and the channel current is approximately 2 A [around 23–27 ns in Fig. 13(a)]. In the case of $V_{th} = 1.3$ V, the lateral depletion process between the n-pillar and the p-pillar is relatively slower than that of $V_{th} = 3.0$ V. Therefore, the displacement current (I_{P+}) rises to near 4 A to charge C_{DS}, while the channel current drops to 4 A [around 37–40 ns in Fig. 13(b)]. As in the case of $V_{th} = 3.5$ V, the increasing V_{DS} completely depletes the n-pillar and the p-pillar in the lateral direction. C_{DS} rapidly decreases and the displacement current (I_{P+}) charging C_{DS} is converted into a channel current [around 40 ns in Fig. 13(b)]. At the same time, the gate potential drops to approximately -2 V [around 40 ns in Fig. 13(b)] due to a negative "potential shift" in the gate by $L_S \times dI_S/dt$. This has less negative potential shift than the $V_{th} = 3.5$ V case. This is because, as mentioned above, the low threshold voltage condition leads to a low gate discharge current. The low threshold voltage causes the channel to close relatively slow speed and results in a slow decrease in the source current (I_S as well as $L_S \times dI_S/dt$).

VI. CONCLUSION

The gate ringing of superjunction MOSFETs after gamma-ray irradiation was analyzed. To provide an accurate physical analysis, mixed-mode simulated waveforms with a threshold voltage (1.3 and 3.5 V) were compared with the the actual measured waveforms.

During the turn-on transient, primary gate ringing and secondary gate ringing occurred. Primary gate ringing experienced a positive "potential shift" due to the back electromotive force on the parasitic source inductance when the channel was formed and the source current flowed. This caused a rapid change in the gate voltage and a rapid decrease in the gate current dI_G/dt. Therefore, the parasitic gate inductance $L_G \times dI_G/dt$ and C_{ISS} combined to generate primary gate ringing. Secondary gate ringing occurred when the displacement current of the freewheeling diode decreased. The MOSFETs experienced a negative "potential shift" due to the reverse electromotive force of the parasitic source inductance. In the case of a low threshold voltage ($V_{th} = 1.3$ V), dI_S/dt was high, and it experienced more negative "potential shift." Therefore, the rapid change in gate voltage and the rapid increase in gate current dI_G/dt led to a prominent gate ringing.

In the case of the turn-off transient, gate ringing of the gamma-ray irradiated devices was relatively small compared to the normal device. Gamma-ray irradiated devices had a lower V_{GP} because they had a smaller threshold voltage than nonirradiated devices. This causes a slow gate discharging current. Therefore, the source current (I_S) decreased slowly (low dI_S/dt) because the channel closed slowly. The low dI_S/dt results in a low "potential shift" of the parasitic source inductance. Finally, the gate voltage had a low negative "potential shift" and a small gate ringing.

REFERENCES

[1] B. K. Bose, "Evaluation of modern power semiconductor devices and future trends of converters," *IEEE Trans. Ind. Appl.*, vol. 28, no. 2, pp. 403–413, Apr. 1992.

[2] B. J. Baliga, "The future of power semiconductor device technology," *Proc. IEEE*, vol. 89, no. 6, pp. 822–832, Jun. 2001, doi: 10.1109/5.931471.

[3] P. Bowler, "Semiconductor power devices," *Electron. Power*, vol. 24, no. 8, pp. 9–59, Aug. 1978.

[4] M. D. Kankam and M. E. Elbuluk, "A survey of power electronics applications in aerospace technologies," in *Proc. 36th Intersociety Energy Convers. Eng. Conf.*, Dec. 2001, pp. 1–13.

[5] A. J. Wileman, S. Aslam, and S. Perinpanayagam, "A road map for reliable power electronics for more electric aircraft," *Prog. Aerosp. Sci.*, vol. 127, Nov. 2021, Art. no. 100739, doi: 10.1016/j.paerosci.2021.100739.

[6] R. Sujatha, R. Damle, A. R. Khan, and M. Ravindra, "Study of the effect of gamma radiation on MOSFET for space applications," *Indian J. Pure Appl. Phys.*, vol. 56, no. 8, pp. 587–590, 2018.

[7] K. Gao, Y. Chen, S. Zheng, M. Liao, X. Xu, and M. Lu, "Degradation behavior and mechanism of SiC power MOSFETs by total ionizing dose irradiation under different gate voltages," in *Proc. IEEE Workshop Wide Bandgap Power Devices Appl. Asia*, Wuhan, China, Aug. 2021, pp. 46–50, doi: 10.1109/WiPDAAsia51810.2021.9656082.

[8] P. J. Wahle, R. D. Schrimpf, and K. F. Galloway, "Simulated space radiation effects on power MOSFETs in switching power supplies," *IEEE Trans. Ind. Appl.*, vol. 26, no. 4, pp. 798–802, Aug. 1990, doi: 10.1109/28.56008.

[9] R. W. Tallon, M. R. Ackermann, W. T. Kemp, M. H. Owen, and D. P. Saunders, "A comparison of ionizing radiation damage in MOSFETs from cobalt-60 gamma rays, 0.5 tO 22 MeV protons and 1 to 7 MeV electrons," *IEEE Trans. Nucl. Sci.*, vols. NS-32, no. 6, pp. 4393–4398, Dec. 1985, doi: 10.1109/TNS.1985.4334130.

[10] T. R. Oldham and F. B. McLean, "Total ionizing dose effects in MOS oxides and devices," *IEEE Trans. Nucl. Sci.*, vol. 50, no. 3, pp. 483–499, Jun. 2003.

[11] M. R. Shaneyfelt, D. M. Fleetwood, J. R. Schwank, and K. L. Hughes, "Charge yield for cobalt-60 and 10-keV X-ray irradiations of MOS devices," *IEEE Trans. Nucl. Sci.*, vol. 38, no. 6, pp. 1187–1194, Dec. 1991.

[12] J. R. Schwank et al., "Radiation effects in MOS oxides," *IEEE Trans. Nucl. Sci.*, vol. 55, no. 4, pp. 1833–1853, Aug. 2008.

[13] E. H. Poindexter. (1989). *MOS Interface States: Overview and Physicochemical Perspective*. [Online]. Available: http://iopscience.iop.org/0268-1242/4/12/001

[14] F. Udrea, G. Deboy, and T. Fujihira, "Superjunction power devices, history, development, and future prospects," *IEEE Trans. Electron Devices*, vol. 64, no. 3, pp. 713–727, Mar. 2017, doi: 10.1109/TED.2017.2658344.

[15] Infineon Technology, "Parasitic turn-on of power MOSFET—How to avoid it?" Appl. Note, 2008. [Online]. Available: https://www.infineon.com/dgdlac/Infineon-Parasitic_Turn-on_of_Power_MOSFET-ApplicationNotes-v01_00-EN.pdf?fileId=db3a30431ed1d7b2011eee756cee5475

[16] I. Castro et al., "Analytical switching loss model for superjunction MOSFET with capacitive nonlinearities and displacement currents for DC–DC power converters," *IEEE Trans. Power Electron.*, vol. 31, no. 3, pp. 2485–2495, Mar. 2016, doi: 10.1109/TPEL.2015.2433017.

[17] H. Kang and F. Udrea, "True origin of gate ringing in superjunction MOSFETs: Device view," *IEEE Trans. Power Electron.*, vol. 36, no. 5, pp. 5362–5370, May 2021, doi: 10.1109/TPEL.2020.3027663.

[18] P. J. McWhorter and P. S. Winokur, "Simple technique for separating the effects of interface traps and trapped-oxide charge in metal-oxide-semiconductor transistors," *Appl. Phys. Lett.*, vol. 48, no. 2, pp. 133–135, Jan. 1986, doi: 10.1063/1.96974.

[19] X. Li et al., "Degradation in super-junction MOSFET under successive exposure of heavy ion strike and gamma ray irradiation," *Microelectron. Rel.*, vol. 132, May 2022, Art. no. 114529, doi: 10.1016/j.microrel.2022.114529.

[20] T. Sakai and T. Yachi, "Effects of gamma-ray irradiation on thin-gate-oxide VDMOSFET characteristics," *IEEE Trans. Electron Devices*, vol. 38, no. 6, pp. 1510–1515, Jun. 1991.

[21] B. J. Baliga, *Fundamentals of Power Semiconductor Devices*. Cham, Switzerland: Springer, Apr. 2010.

[22] H. Kang and F. Udrea, "Gate ringing in superjunction MOSFETs with a parasitic capacitance in the load inductor," *Power Electron. Devices Compon.*, vol. 4, Mar. 2023, Art. no. 100029, doi: 10.1016/j.pedc.2022.100029.